Study on thermal control strategy of integrated thermal management system for electric vehicle

Qiping Chen[1], Chan Xu[1,2], Senhai Liu[2], Chenping Zhong[2], Xiaochun Zeng[2], Xianzhong Yu[2]

[1]School of Mechatronics & Vehicle Engineering, East China Jiaotong University, Nanchang, China

[2]Jiangling Motor Co., Ltd., Nanchang, China

Corresponding author: Qiping Chen, School of Mechatronics & Vehicle Engineering, East China Jiaotong University, Nanchang 330013, China ; Chan Xu, School of Mechatronics & Vehicle Engineering, East China Jiaotong University, Nanchang 330013, China.

Email: qiping3846758@163.com

ABSTRACT: To address the challenges of poor temperature control precision in electric vehicle battery and cabin, as well as high overall energy consumption, an innovative control strategy for an integrated thermal management system (ITMS) is proposed. Through systematic analysis of the thermal management system's (TMS) dynamic characteristics and intricate coupling relationships, critical control requirements for battery and cabin thermal management were identified. A novel deep learning model, integrating a convolutional neural network (CNN) and a long short-term memory (LSTM) network, is developed. This unique architecture effectively extracts spatiotemporal features, enabling precise temperature trend prediction and adaptive control. Simulation results demonstrate significant improvements over conventional PID control. Thermal stabilization was reduced by approximately 40–43%. Temperature control precision was enhanced to within ±0.3°C across diverse operating conditions, while compressor energy consumption was significantly decreased. These advancements resulted in an average 2.1% increase in energy efficiency coefficient and a 1.8% improvement in exergy efficiency, accompanied by a substantial reduction in performance fluctuations. Simulation evaluations across the new European driving cycle (NEDC), worldwide harmonized light vehicles test cycle (WLTC), and China light-duty vehicle test cycle (CLTC) confirm the superiority of the proposed CNN-LSTM strategy in temperature regulation, energy utilization, and system stability. This approach provides an effective solution for optimizing next-generation TMS for electric vehicle.

Keywords: Electric vehicle, Integrated thermal management systems, CNN-LSTM

1. Introduction

1.1 Motivations

Amidst escalating global energy concerns and environmental degradation, electric vehicles (EVs) have emerged as a promising sustainable transportation solution. Central to their successful operation in an efficient thermal management system (TMS)[1], [2]. While direct battery cooling offers advantages, its integration with the air conditioning system can present challenges[3]. Existing control strategies, including proportional-integral-derivative (PID) control, fuzzy logic control (FLC), and model predictive control (MPC), exhibit limitations, such as instability, sluggish response, and temperature fluctuations[4], [5], [6]. These shortcomings not only impact passenger comfort but also compromise battery lifespan and overall system reliability[7], [8]. Moreover, conventional approaches struggle to adapt effectively to dynamic thermal loads, leading to suboptimal energy consumption and reduced system efficiency.

Preprint not peer reviewed

This preprint research paper has not been peer reviewed. Electronic copy available at: https://ssrn.com/abstract=5134166

This study introduces a novel integrated TMS control strategy utilizing a convolutional neural network (CNN)-LSTM architecture. By synergistically combining the spatial feature extraction capabilities of CNNs with the temporal prediction prowess of long short-term memory (LSTM) networks, this approach enables accurate temperature forecasting and precise TMS control. The efficacy of this proposed strategy is rigorously validated through comprehensive co-simulation studies conducted on the Amesim and MATLAB platforms. This study endeavors to enhance both the thermal performance and energy efficiency of EVs, offering valuable technical insights for future EV development.

1.2 Research review

TMS is paramount for optimal EV performance and passenger comfort. Recent research has significantly advanced the integrated thermal management of battery and air conditioning systems. From the perspective of system architecture, Guo et al. [9]introduced a novel refrigerant-based TMS with a postpositional throttle valve, enabling independent temperature control for both the battery and cabin while directly heating/cooling the battery. This design demonstrated enhanced thermal comfort and battery safety, including 15-minute battery preheating in winter. Similarly, Gao et al.[3]decoupled cooling and control through structural design, introducing a preconditioning framework that mitigated the detrimental effects of high thermal inertia on system performance. However, both studies lack comprehensive validation under diverse operating conditions.

In terms of control strategy optimization, Xu et al.[10]refined the control approach by implementing advanced algorithms for high-precision temperature control and optimized refrigerant distribution. Furthermore, MPC-based control strategies developed by Wang et al.[11]and He et al.[12]have been experimentally validated for optimizing energy consumption and thermal comfort within this integrated framework. While these control strategies show promise, they face challenges in real-time implementation due to computational complexity.

Moving towards system integration, Ma et al. [13]developed an integrated TMS that effectively maintained optimal temperature ranges for batteries, motors, and the passenger cabin. Zhang et al. [14]developed a coordinated control strategy for cooling capacity allocation, resulting in a significant improvement in the system's coefficient of performance. Wang et al.[15] and Fei et al. [16]explored the potential of carbon dioxide-based TMS in conjunction with neural network-based control strategies, demonstrating significant enhancements in system energy efficiency and temperature control precision. However, these integrated approaches often struggle with system reliability and maintenance complexity.

In summary, optimizing EV TMS presents a multifaceted challenge that necessitates a multidisciplinary approach encompassing control theory, materials science, and thermodynamics. Future research endeavors should concentrate on further exploring the interdisciplinary connections between these fields to develop more efficient and environmentally sustainable TMS solutions.

1.3 Contributions

The paper presents the following key contributions.

(1) An innovative integrated TMS control strategy utilizing a CNN-LSTM architecture is introduced. This approach demonstrates exceptional capabilities in accurately predicting battery temperature trends and executing precise TMS control actions. Notably, the proposed strategy achieves temperature control precision within ±0.3°C across diverse operating conditions, representing a significant advancement over conventional control methods.

(2) A novel CNN-LSTM model is proposed and its performance systematically compared against existing state-of-the-art control algorithms. Through rigorous co-simulation conducted within the Amesim and MATLAB software environments, the proposed strategy demonstrates remarkable improvements in multiple performance metrics. Specifically, the results show a 40-43% reduction in thermal stabilization time, accompanied by a 2.1% increase in energy efficiency coefficient and a 1.8% enhancement in exergy efficiency. Additionally, the strategy achieves significant reductions in both compressor energy consumption and performance fluctuations, highlighting its superior control capabilities.

(3) A thorough analysis of the proposed control strategy's potential applications reveals its capacity to significantly enhance the thermal management performance and energy efficiency of EVs, thereby facilitating their further development.

1.4 Organization of this article

Preprint not peer reviewed

This preprint research paper has not been peer reviewed. Electronic copy available at: https://ssrn.com/abstract=5134166

The rest of this paper is structured as follows. Section II provides an overview of the theoretical foundations and relevant prior work. Section III details the construction and training process of the CNN-LSTM model. Section IV presents the results of co-simulation experiments conducted utilizing MATLAB and Amesim. A comprehensive discussion of the findings presented in Sections III and IV is provided in Section V. Finally, Section VI concludes the paper and outlines potential avenues for future research.

2. Theoretical analysis of thermal management

2.1 System description and analysis

The integrated thermal management system (ITMS), depicted in Fig. 1, incorporates a sophisticated dual-loop architecture that seamlessly integrates refrigerant and water-glycol coolant circuits to precisely regulate temperatures across all EV subsystems. The system operates in two distinct modes: summer cooling and winter heating, with seamless transitions facilitated by advanced control of the expansion valve (EXV) and a variable-speed electronic pump. Key components within this system encompass a high-efficiency compressor, a bidirectional internal heat exchanger, a multi-functional condenser, a high-performance chiller, and a dedicated motor radiator. The bidirectional internal heat exchanger plays a pivotal role in both operational modes. In summer, it facilitates heat rejection from the hot refrigerant loop, while in winter, it enables heat pump operation by effectively transferring waste heat from the refrigerant cycle to the cabin heating loop, thereby enhancing overall energy efficiency. The chiller is directly integrated with the battery cooling system, providing dedicated thermal management for high-voltage batteries. In summer mode, it collaborates with the evaporator to effectively dissipate excess heat from the battery pack, ensuring optimal operating conditions and maintaining system safety. In winter mode, it preheats the battery for operation in low-temperature environments, utilizing waste heat recovered from other subsystems. The motor radiator actively cools the electric powertrain, maintaining its stability under extreme workloads. Subsequently, the system circulates the heat-exchanging water-glycol coolant through the conventional radiator to dissipate heat generated by the motor, utilizing an electronic pump to facilitate coolant circulation. The electronic pump operates dynamically, adjusting the coolant flow rate through the radiator based on thermal demands.

The system incorporates two EXVs for enhanced thermal control precision. The battery EXV regulates refrigerant flow to the battery cooling system, providing both cooling and heating as required. Simultaneously, the cabin EXV maintains optimal cabin climate, prioritizing passenger comfort and energy efficiency. In winter mode, an advanced heat pump system efficiently recovers waste heat generated by the motor and compressor. This recovered heat is subsequently redistributed to the cabin and battery subsystems via the integrated refrigerant and coolant circuits. This integrated approach minimizes energy consumption while ensuring optimal passenger comfort and battery performance in colder weather conditions. This advanced system design constitutes a significant technological advancement in EV thermal management. By strategically cascading heat utilization across subsystems, the system achieves exceptional energy efficiency and environmental adaptability. To address the complexities inherent in managing the thermal profiles of batteries, electric powertrains, and cabins, advanced control algorithms are implemented through electronic EXVs and a variable-speed pump, enabling precise thermal control. This pioneering architecture approach redefines the benchmark for thermal management technology in EVs.

Preprint not peer reviewed

This preprint research paper has not been peer reviewed. Electronic copy available at: https://ssrn.com/abstract=5134166

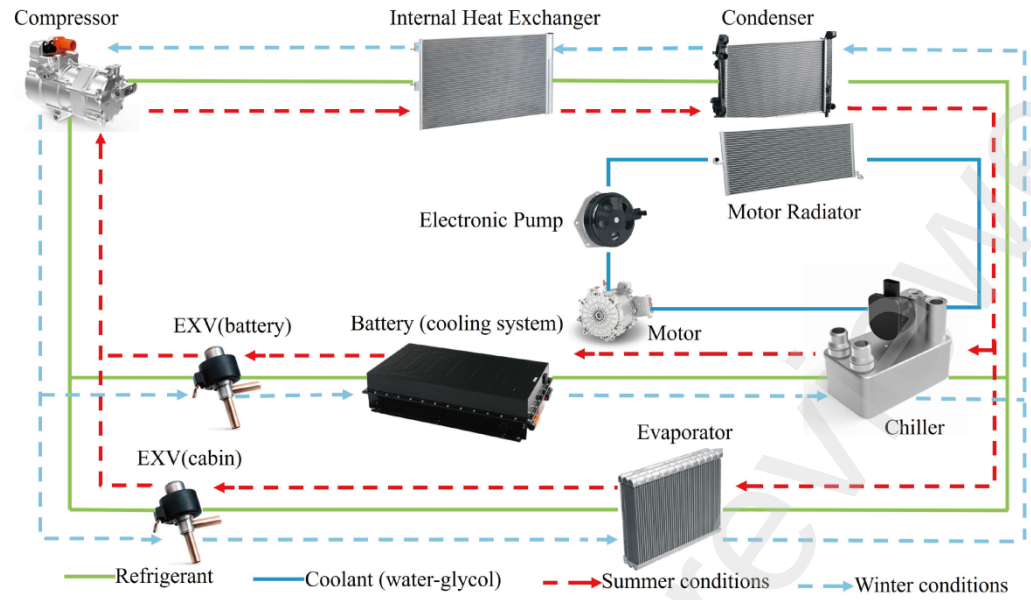

Fig. 1 Integrity thermal management system diagram

2.2 Design of theoretical framework for hybrid CNN-LSTM architecture

Contemporary research in TMS frequently encounters limitations when employing traditional control theory to accurately model and predict the dynamics of intricate systems. To overcome these challenges, this study proposes a CNN-LSTM model as a robust solution for ITMS. By effectively integrating the spatial feature extraction capabilities of CNNs with the temporal modeling prowess of LSTM networks, this model excels at processing multivariate spatiotemporal data. This unique architecture enables the efficient handling of complex control challenges, thereby enhancing the precision and adaptability of TMS systems.

CNNs are a class of deep learning models specifically designed for processing grid-structured data, such as images. They employ convolutional layers, which utilize multiple kernels to extract spatial features by computing weighted sums of local regions within the input data[17]. This architecture, characterized by local connectivity and weight sharing, results in efficient parameter utilization and improved computational performance, particularly in image processing[18]. In the context of TMS, CNNs can be effectively leveraged to learn and recognize distinct temperature distribution patterns within both battery systems and cabin air conditioning systems. This enables the generation of more comprehensive feature representations, which can then be utilized to inform and optimize subsequent control decisions. By analyzing temperature distributions, CNNs can identify regions of significant heat accumulation, thereby facilitating data-driven optimization of cooling strategies.

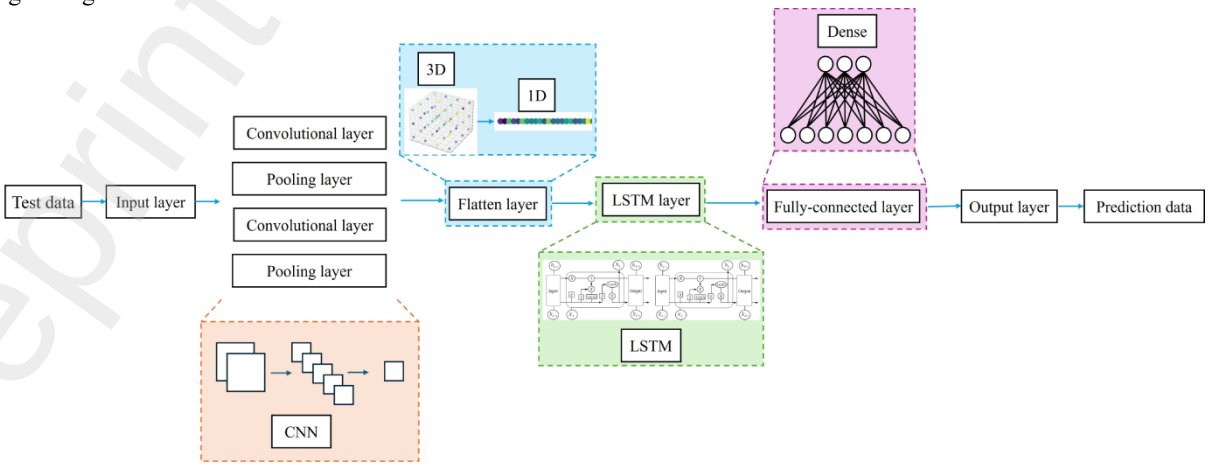

Fig. 2 Architectural diagram of CNN-LSTM model

LSTM networks, a specialized class of recurrent neural networks (RNNs), have been specifically

Preprint not peer reviewed

This preprint research paper has not been peer reviewed. Electronic copy available at: https://ssrn.com/abstract=5134166

designed to address the vanishing and exploding gradient problems commonly encountered by traditional RNNs when processing extended sequences[19]. LSTMs incorporate gated mechanisms: input, forget, and output gates, to regulate the flow of information. This architectural innovation enables the network to effectively capture and maintain long-range dependencies within sequential data. The core mechanism of the LSTM architecture is mathematically represented as follows[20]:

$$f_t = \sigma(W_f \bullet [h_{t-1}, X_t] + b_f) \tag{1}$$

$$i_t = \sigma(W_i \bullet [h_{t-1}, X_t] + b_i) \tag{2}$$

$$o_t = \sigma(W_o \bullet [h_{t-1}, X_t] + b_o) \tag{3}$$

$$\dot{C}_t = tanh(W_C g[h_{t-1}, X_t] + b_C) \tag{4}$$

$$C_t = f_t \times C_{t-1} + i_t \times \tilde{C}_t \tag{5}$$

$$h_t = o_t \times tanh(C_t) \tag{6}$$

where f_t denotes the forget gate output, i_t signifies the input gate output, o_t represents the output gate output, C_t indicates the candidate state output, C_t articulates the cell state update output, and h_t represents the hidden state update output. σ denotes the Sigmoid activation function, W_f and b_f signify the weights and bias of the forget gate, respectively, W_i and b_i indicates the weights and bias of the input gate, respectively, and W_o and b_o denote the weights and bias of the output gate, respectively. $tanh$ indicates the tanh activation function, and W_C and b_C exemplify the weights and bias of the candidate state, respectively.

This study employs a CNN-LSTM architecture, combining the strengths of CNNs for spatial feature extraction and LSTM for temporal analysis. This integrated approach enables the model to effectively process spatiotemporal data, as demonstrated in previous studies[21], [22]. By initially extracting spatial features with CNNs and subsequently feeding these features into an LSTM for temporal modeling[23], the model effectively captures both spatial and temporal dynamics. This architecture proves particularly well-suited for addressing complexities inherent in TMS control problems.

Fig. 2 depicts the CNN-LSTM architecture employed for spatiotemporal data processing within the ITMS framework. The initial stage involves the processing of test data, followed by its input into a CNN module consisting of two sequential blocks of convolutional and pooling layers. This hierarchical design facilitates multi-scale feature extraction, capturing both local and global spatial patterns within the thermal data. Subsequently, a flattened layer transforms the 3D spatial features into a 1D vector, ensuring compatibility with the subsequent LSTM module. The LSTM layer, equipped with gating mechanisms, effectively captures temporal dependencies, enabling accurate prediction of dynamic variables, including temperature fluctuations, current variations, and voltage changes. Finally, a fully connected layer with learnable weights maps the high-dimensional LSTM features into task-specific representations. This non-linear mapping enables accurate prediction of critical thermal management parameters. The output layer generates the final predictions, providing valuable insights for real-time control decisions. This modular architecture allows for end-to-end training while maintaining a distinct separation between spatial and temporal feature processing, thereby enhancing model interpretability and optimization flexibility. By integrating the hierarchical feature extraction capabilities of CNNs with the temporal modeling capabilities of LSTMs, this framework provides a robust solution for addressing complex, multivariable thermal management challenges. This ultimately contributes to improved battery safety, enhanced energy efficiency, and enhanced passenger comfort.

In conclusion, the CNN-LSTM model, demonstrating exceptional spatiotemporal feature extraction and prediction capabilities, provides a robust theoretical foundation for ITMS[24]. Future research endeavors should concentrate on optimizing the model's architecture and training methodologies. This may involve incorporating attention mechanisms or exploring multi-task learning frameworks to further enhance prediction accuracy and real-time performance[25]. Furthermore, by integrating operational data from real-world TMS applications and continuously refining the CNN-LSTM model, more reliable technical support can be effectively provided for the intelligent control of TMSs in the context of new energy vehicles.

3. CNN-LSTM model: construction and training

Preprint not peer reviewed

This preprint research paper has not been peer reviewed. Electronic copy available at: https://ssrn.com/abstract=5134166

This section provides a detailed description of the CNN-LSTM model architecture, encompassing data acquisition protocols, variable preprocessing techniques, and optimization strategies. Specific model parameters are included to facilitate reproducibility.

3.1 Model construction

The proposed CNN-LSTM architecture employs a two-stage pipeline. In the initial stage, a CNN component, consisting of two convolutional layers with 32 and 64 filters respectively, extracts spatial features from diverse input parameters, encompassing light intensity, battery system electrical characteristics, and thermal measurements. Subsequently, a 64-neuron LSTM layer processes these extracted features to identify temporal patterns, as show in Fig.3.

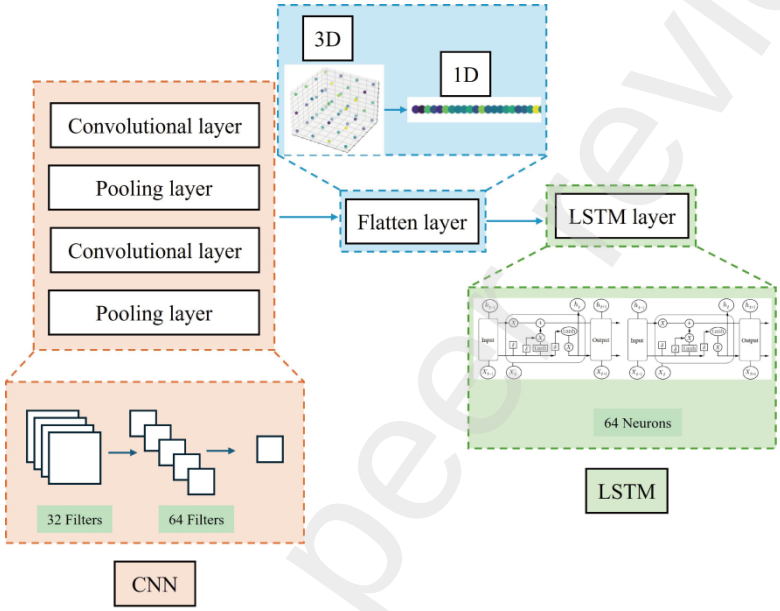

Fig. 3 Diagram of CNN and LSTM layer

3.2 Data acquisition

This investigation utilizes a comprehensive dataset acquired through a rigorous series of summer trials conducted in the Turpan region of Xinjiang, a location characterized by an extreme continental desert climate. The experimental campaign, spanning from June to August 2024, encompassed ambient temperatures ranging from 25 to 55°C and relative humidity levels between 10% and 30%, thereby providing optimal conditions for TMS evaluation.

Data acquisition employed a high-precision measurement system. Electrical parameters, such as current and voltage, were sampled at 10 Hz with ±0.1% accuracy. Thermal measurements were recorded at 1 Hz with ±0.5°C accuracy, and solar radiation intensity was monitored at 1 Hz with ±1 W/m^2 accuracy. The EXV positions were tracked at 10 Hz with a 0.1% resolution, and compressor rotational speed was measured at 10 Hz with ±1 rpm accuracy. Data collection adhered to rigorous scientific protocols and industry best practices to ensure data integrity and reliability. All testing was performed at professional facilities under the supervision of experienced engineers utilizing state-of-the-art equipment. Vehicles were subjected to a range of environmental conditions, including high temperatures and extreme aridity, to simulate real-world operational scenarios.

To safeguard proprietary information and intellectual property, the specific identity of the collaborating automotive company will remain undisclosed. All data utilization has been duly authorized by the company and strictly adheres to the provisions of the applicable data usage agreements and confidentiality obligations.

3.3 Input and output variables

Precise control of the battery system EXV, cabin EXV, and compressor rotational speed is crucial to

Preprint not peer reviewed

This preprint research paper has not been peer reviewed. Electronic copy available at: https://ssrn.com/abstract=5134166

simultaneously optimize battery performance, safety, and passenger thermal comfort. To facilitate rapid response to battery system thermal management demands, the system employs dual EXVs and a refrigerant receiver. The model incorporates the following input variables: solar radiation intensity (Sunload), battery system current (BatCurrent), battery system voltage (BatVol), ambient temperature (AmbTemp), cabin temperature (CabTemp), and battery temperature (BatTemp). The output variables comprise battery system EXV opening (BatEXV), cabin EXV opening (CabEXV), and compressor rotational speed (ComSpd). To mitigate the influence of disparate variable magnitudes on model learning and training efficiency, normalization is applied to all variables except for EXV openings. The normalization formula is presented below:

$$X_{\text{norm}} = \frac{X - X_{\min}}{X_{\max} - X_{\min}} \tag{7}$$

where X_{norm} represents the normalized value, X denotes the original value, X_{min} signifies the minimum value within the data series, and X_{max} specifies the maximum value within the data series.

The normalization formula specifically for EXV opening is presented below:

$$K_{\text{norm}} = \frac{K}{K_{\max}} \tag{8}$$

where K_{norm} denotes the normalized value, K signifies the original value, and K_{max} corresponds to the value at 100% EXV opening.

3.4 Optimization algorithms and activation functions

The Adam optimization algorithm is widely recognized for its efficiency and stability in training deep learning models[26], [27]. This study employs the Adam algorithm to optimize the CNN-LSTM model. By calculating exponentially decaying averages of the first and second moments of the gradients, Adam adaptively adjusts the learning rate for each parameter, facilitating dynamic balance during training[28], [29]. Furthermore, by incorporating both momentum and variance of gradients, Adam typically exhibits faster convergence compared to traditional stochastic gradient descent (SGD)[30].

Activation functions enable neurons to learn and map features to the model's output in a functional form. The ReLU function was selected as the activation function for this model. Model parameter settings are summarized in Table 1.

Table 1

CNN-LSTM model hyperparameters

Parameter	Value
Number of kernels in the first convolutional layer	32
Number of kernels in the second convolutional layer	64
Number of convolutional layers	2
Batch size	128
Stride	1
Number of LSTM layers	1
Number of fully connected layers	1
Number of neurons in the LSTM cell	64

Preprint not peer reviewed

This preprint research paper has not been peer reviewed. Electronic copy available at: https://ssrn.com/abstract=5134166

3.5 Training process and validation

The CNN-LSTM model exhibited distinct optimization characteristics throughout its training, demonstrating three primary convergence phases, as depicted in Fig. 4. The first 50 epochs demonstrated a distinct descent phase, characterized by a consistent decay rate of 0.092 per epoch, with concurrent convergence patterns in both training and validation losses. Subsequently, an intermediate stabilization phase emerged, characterized by damped oscillations with an amplitude reduction from 0.04 to 0.01 and featuring three characteristic intersection points between training and validation curves. This phase suggests inherent self-regularizing properties within the model. Finally, the model entered a convergence phase with remarkable stability, exhibiting minimal divergence between training and validation metrics and terminal loss fluctuations confined within 0.001.

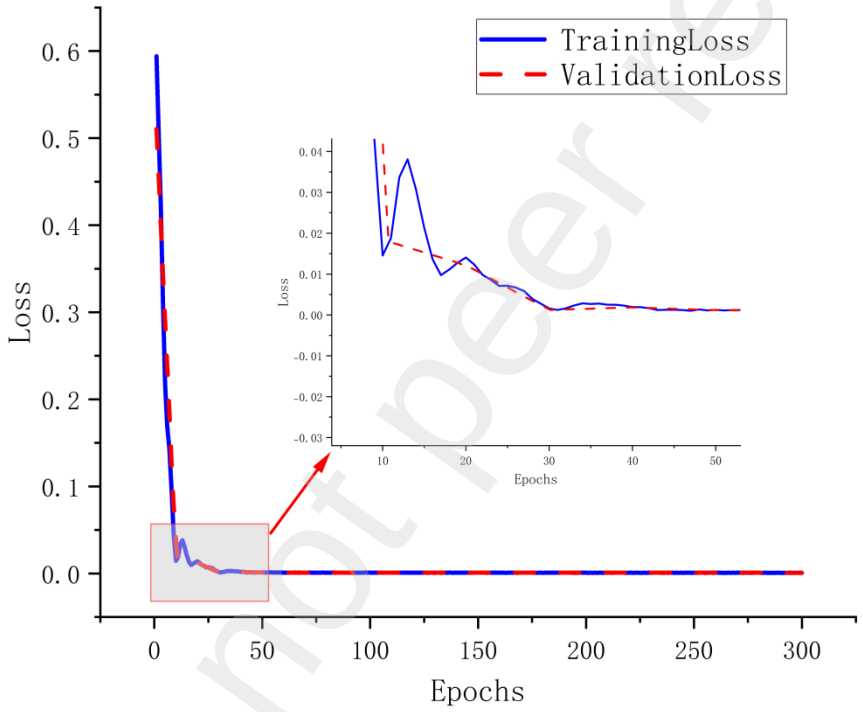

Fig. 4 Training and validation loss curves for the CNN-LSTM model

Validation results for battery EXV control exhibited exceptional predictive accuracy within an 800-second operational window, as illustrated in Fig. 5(a). The model demonstrated precise tracking of valve positions within a range of 115 to 161 units, achieving an R^2 coefficient exceeding 0.998 and maintaining a mean absolute deviation of 0.5 units. This performance encompassed accurate representation of both transient and steady-state behaviors, thereby indicating robust control capabilities across a diverse range of operational conditions.

Validation results for cabin EXV control, as depicted in Fig. 5(b), exhibited three distinct operational periods, each characterized by unique dynamic behavior. An initial adaptation phase (0–200 seconds) was observed, featuring minor prediction oscillations around 145 units and effectively mitigating early-stage uncertainties. This was followed by an intermediate period (200–600 seconds) characterized by complex three-stage behavior patterns within an operational range of 134 to 166 units, demonstrating high-fidelity tracking during rapid transitions. Finally, a terminal period (600–800 seconds) emerged, exhibiting controlled descent characteristics with a mean absolute error below 1.5 units and demonstrating sophisticated non-linear response patterns.

Validation results for compressor speed control, as illustrated in Fig. 5(c), further substantiated the

Preprint not peer reviewed

This preprint research paper has not been peer reviewed. Electronic copy available at: https://ssrn.com/abstract=5134166

model's capabilities within an operational range of 5900–6080 rpm. The prediction system maintained error margins below 5 rpm while exhibiting exceptional accuracy during dynamic transitions. This performance validates the model's robust capacity to handle varying load conditions and complex system dynamics.

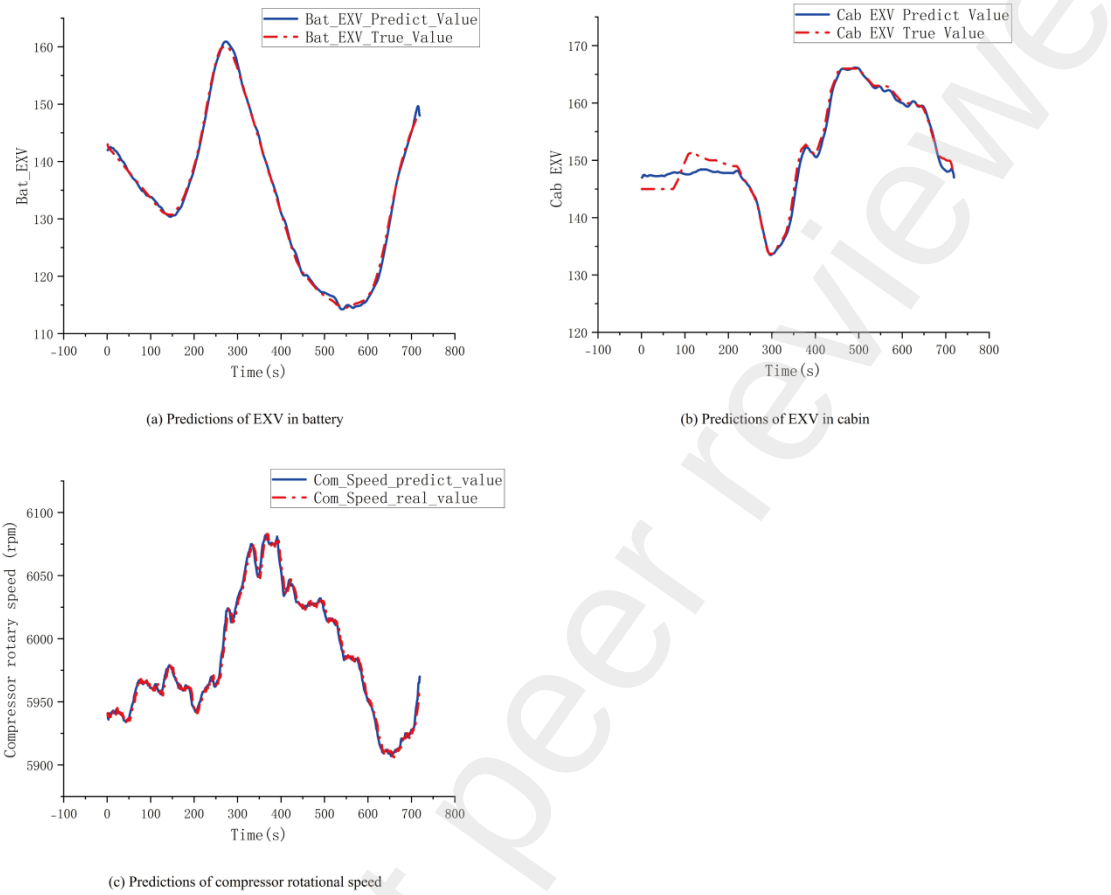

(a) Predictions of EXV in battery

(b) Predictions of EXV in cabin

(c) Predictions of compressor rotational speed

Fig. 5 Predictive performance of dual-EXV positions and compressor speed within the TMS

Comprehensive validation results unequivocally demonstrate superior control capabilities across multiple parameters. The model consistently exhibited high-fidelity performance with sub-1% error margins during steady-state operations, accurately capturing dynamic system behaviors while maintaining reliable long-term prediction stability. These characteristics were particularly evident in the system's adaptability to varying operational conditions and its robust performance during rapid state transitions, characterized by minimal latency in control adjustments.

The model’s predictive capabilities were rigorously validated through extensive testing and analysis, demonstrating its suitability for practical thermal management applications. These findings provide a strong foundation for subsequent system implementation and optimization efforts. The demonstrated performance metrics strongly suggest significant potential for enhancing the efficiency and control precision of TMSs in real-world scenarios.

This validation phase unequivocally demonstrates the model’s readiness for practical implementation, surpassing the performance of conventional control methodologies. Subsequent chapters will delve into the practical implementation of this validated model within TMSs, evaluating its performance across diverse operating conditions and real-world scenarios.

4. Simulation experiments

A co-simulation framework integrating MATLAB and Amesim was developed to simulate the vehicle’s TMS. Control strategies were implemented within the MATLAB environment, while the TMS model was constructed using Amesim. A hierarchical structure facilitated the integration of these sub-models, enabling the capture of complex thermal interactions between subsystems. The battery thermal model and cabin model exchanged data at each time step through the refrigeration cycle model, serving as the primary coupling

Preprint not peer reviewed

This preprint research paper has not been peer reviewed. Electronic copy available at: https://ssrn.com/abstract=5134166

interface. To ensure both numerical stability and computational efficiency, a variable time-step solver was employed, with a maximum step size of 0.1 seconds and a minimum step size of 0. 01 seconds.

The system and its constituent components were meticulously designed and selected to align with the research objectives. This culminated in the development of both a comprehensive numerical model and an experimental setup for the TMS. The numerical model integrates detailed heat transfer mechanisms and fluid dynamics while maintaining a computationally tractable level of complexity. The specifications of the experimental system components are presented in Table 2.

Table 2

Parameters of the numerical model and experimental system

Components	Parameters	Unit
Refrigerant	R134a	/
Compressor	Type: Electric scroll	/
	Displacement: 45 cc/rev	cc/rev
	Speed range: 1000–7000	rpm
	Max. cooling capacity: 8	kW
Condenser	Material: Aluminum	/
	Type: Parallel flow	/
	Size (L*H*T) fin area: 695 × 437 × 16	mm
	Number of passes: 4	/
	Number of tubes for each pass: 26, 18, 12, 7	/
	Fin thickness: 0.09	mm
	Fin pitch: 2.6	mm
Evaporator	Material: Aluminum	/
	Type: Plate-fin	/
	Size(L*H*T) fin area: 259.6 × 216.2 × 38	mm
	Number of passes: 4	/
	Number of tubes for each pass: 19, 19,19,19	/
	Fin thickness: 0.06	mm
	Fin pitch: 2.8	mm

An accurate representation of the passenger cabin and battery system within the system model is crucial for the successful construction of a simulation model.

4.1 Design of Cabin model

A 3D computational fluid dynamics (CFD) offers a comprehensive understanding of temperature fields and heat flux distributions within vehicle cabins. Concurrently, the computational demands of CFD models pose significant obstacles for real-time control applications[31]. To overcome these limitations, this study

Preprint not peer reviewed

This preprint research paper has not been peer reviewed. Electronic copy available at: https://ssrn.com/abstract=5134166

employs a simplified lumped-parameter approach. A 1D model is utilized to characterize the cabin's thermal behavior[32], treating it as a single thermodynamic system containing moist air. The following key assumptions underpin this model [33]:

The analysis assumes the three simplifications: (1) the constant thermophysical properties of all structural materials, including the roof and windows; (2) the uniform spatial geometry and temperature distribution, neglecting geometric complexities and spatial thermal variations; and (3) the constant air density and specific heat capacity under operating conditions.

A comprehensive heat transfer framework models the thermal interactions between the cabin and its environment. This framework encompasses both external environmental heat exchange and internal air-material interactions[34]. Table 3 details the physical specifications of the experimental cabin, while Table 4 summarizes the governing equations and heat transfer relationships.

Table 3

Cabin parameters and specifications

Components	Parameters	Unit
Cabin volume	4.35	m^3
Cabin initial relative humidity	40%	/
Wall thermal capacity	7000	J/°C
Internal exchange surface	16.2	m^2
External exchange surface	16.2	m^2
External temperature	38	°C
External pressure	1.013	barA
External relative humidity	40%	/
Solar flux	1000	W/m^2
Solar flux absorption coefficient	0.8	/
Internal aerodynamic coefficient	20	/
Passengers' water production	0	g/hr

Table 4

Computational model of cabin dynamics

Components	Computational equations
External heat transfer	$h_{ext} = h_{convext} S_{ext} (T_W - T_{ext})$
Internal heat transfer	$h_{int} = h_{convint} S_{int} (T_W - T_{int})$
Solar radiation	$h_{solar} = \alpha \cdot S_{ext} \cdot q_{solar}$
	which
	$\frac{d(T_W)}{dt} = \frac{(h_{solar} - h_{ext} - h_{int})}{m \times C_p}$
	$h_{forced} = (0.037 \times Re^{0.8} - 871) \times pr^{1/3} \times \frac{\lambda}{D}$

Preprint not peer reviewed

This preprint research paper has not been peer reviewed. Electronic copy available at: https://ssrn.com/abstract=5134166

$$h_{free} = \left[0.68 + 0.67 \times Ra^{0.25} / \left(1 + (0.492/pr)^{0.5625}\right)^{4/9}\right] \times \frac{\lambda}{D}$$

$$Re = V \times \frac{D}{v}$$

$$pr = \frac{\mu \times C_p}{\lambda}$$

$$Ra = \frac{g \times \beta \times (T_W - T_f) \times D^3}{v^2} \times pr$$

4.2 Design of Battery model

Heat generation within battery systems arises from four primary sources: chemical reactions, Joule heating, side reactions, and polarization effects[35]. The total heat generation rate (Q) can be expressed as:

$$Q = Q_r + Q_j + Q_s + Q_p \tag{9}$$

where Q_r represents the chemical reaction heat (J), Q_j denotes the Joule heat (J), Q_s indicates the side reaction heat (J), and Q_p signifies the polarization heat (J).

A comprehensive battery modeling framework has been developed to address the inherent coupling between thermal and electrical dynamics within battery systems[36]. This integrated approach synergistically combines thermal and electrical models to accurately capture the intricate interdependencies within the battery.

The electrical characteristics of the battery are accurately represented by an equivalent circuit model. This model effectively captures both the external dynamic responses and the internal electrochemical processes within the battery[37]. Notably, the model incorporates interdependent relationships between key parameters, namely the open-circuit voltage and internal resistance, which exhibit variations as functions of state of charge, temperature, and operating current, as presented in Eq. (8). Rigorous validation of the model parameters against manufacturer-supplied specifications (Table 5) ensures accurate performance across diverse operating conditions.

Thermal behavior is modeled utilizing the well-established Bernardi formulation, which accurately quantifies the internal heat generation term within the energy conservation equation [38]. The governing equations for specific heat balance subsequently describe the thermal dynamics. To enhance the fidelity of the heat transfer model, a spatially discretized approach is employed, dividing the battery into three longitudinal sections[39]. This discretization strategy efficiently accounts for the inherent thermal inertia observed in practical heat transfer phenomena:

$$\rho C_p \frac{\partial T}{\partial t} = \lambda \nabla^2 T + \frac{I}{V}\left[(U_{ocv} - U) + T\frac{\partial U_{ocv}}{\partial T}\right] \tag{10}$$

where ρ represents the density of the battery material, C_p indicates the specific heat capacity, λ denotes the thermal conductivity. T exemplifies the battery temperature, t specifies time, and $\nabla^2 T$ is the Laplacian of the temperature. I signifies the current flowing through the battery system, V is the volume of the battery system, U_{ocv} articulates the open-circuit voltage, U is the battery system voltage, $T\frac{\partial U_{ocv}}{\partial T}$ represents the temperature influence coefficient.

Table 5

Battery parameter specifications

Components	Parameters	Unit
Battery capacity (1C,23°C)	90	Ah
Battery anode	$LiFePO_4$	/
Battery size	1300×1200×250	mm
Nominal voltage	312	V
Battery mass	600	kg

Preprint not peer reviewed

This preprint research paper has not been peer reviewed. Electronic copy available at: https://ssrn.com/abstract=5134166

Battery architecture	96S × 1P	/
Energy capacity	60	kw·h
Average specific heat	1128.45	J/(kg·K)
Thermal conductivity	1.82	W/(m·K)

4.3 Design of Refrigeration components model

The compressor model is characterized by a performance map encompassing volumetric (η_{vol}), isentropic (η_{is}), and mechanical (η_{mech}) efficiencies[40]. These performance parameters, provided by the manufacturer, are functions of both pressure ratio and compressor rotational speed[41]. Volumetric effectiveness governs mass flow rate, while isentropic and mechanical effectiveness dictate enthalpy change and torque, respectively. The governing equations are summarized in Table 6.

A discretized approach is employed to model heat transfer within the heat exchanger, considering heat exchange across three key interfaces: refrigerant-wall, air-wall, and wall-fin[42]. Evaporation and condensation processes are characterized by resistance and capacitance calculations. Pressure drop in two-phase flow is computed using a homogeneous model, with fluid viscosity determined by the mean volumetric viscosity approach, analogous to single-phase flow[43]. Distinct heat transfer characteristics are observed between single-phase and two-phase flow regimes. In the single-phase regime, laminar flow characterized by orderly fluid motion with minimal turbulence, exhibits lower Nusselt numbers[44]. Conversely, turbulent flow, characterized by significant fluid mixing, exhibits higher Nusselt numbers, quantified using the Gnielinski correlation. For two-phase flow regimes, heat transfer coefficients are determined utilizing established methodologies: the VDI heat atlas approach for evaporation processes and the Cavallini method for condensation phenomena[45].

A four-quadrant diagram, as depicted in Fig. 6[46], comprehensively characterizes the thermal EXV's performance. This diagram elucidates crucial thermodynamic relationships by systematically mapping the interdependencies between key parameters: valve opening and refrigerant state, evaporator outlet pressure and valve opening across varying temperatures, mass flow rate and valve opening, and evaporator outlet temperature and mass flow rate. This comprehensive analysis provides a thorough understanding of the valve's operational behavior across a wide range of operating conditions[47].

Table 6

Governing equations of the numerical model

Components	Computational equations
Compressor	$\eta_{vol} = \dfrac{\dot{m}}{n\rho_s V_{disp}}$
	$\eta_{is} = \dfrac{h_{dis} - h_s}{h_d - h_s}$
	$\eta_{mech} = \dfrac{\dot{m} \times (h_d - h_s)}{n \times \tau}$
Heat exchangers	$\dot{m} = \rho C_q A \sqrt{\dfrac{2\Delta\rho}{\rho}}$
	Single-phase
	Friction factor $f = 8\left[\left(\dfrac{8}{Re}\right)^{12} + \Phi^{1.5}\right]^{\frac{1}{12}}$
	$\Phi = \left(\dfrac{37530}{Re}\right)^{16} + \Gamma^{16}$

Preprint not peer reviewed

This preprint research paper has not been peer reviewed. Electronic copy available at: https://ssrn.com/abstract=5134166

		$\Gamma = 2.457ln\left(\left(\frac{7}{Re}\right)^{0.9} + 0.27\left(\frac{\varepsilon}{D}\right)\right)$
Condensation		
	Laminar regime	$h_{lam} = 3.66 \times \lambda/D$
	Turbulent regime	$h_{turb} = \frac{0.125f \times (Re - 1000) \times pr}{1 + 12.7\sqrt{0.125f}(pr^{2/3} - 1)} \times \frac{\lambda}{D}$
		Two-phase
Friction factor		$f = 0.0056 + \frac{0.5}{Re^{0.32}}$
Condensation		$h = \mathrm{h}_{LO} \times \left[1 - x + x\sqrt{\frac{\rho_l}{\rho_g}}\right]^{\frac{4}{5}}$
		$\mathrm{h}_{LO} = 0.05 \times {Re_{LO}}^{0.8} \times pr^{1/3} \times \frac{\lambda}{D}$
Evaporation		$h = \sqrt[3]{h_{cv}^3 + h_{NcB}^3}$

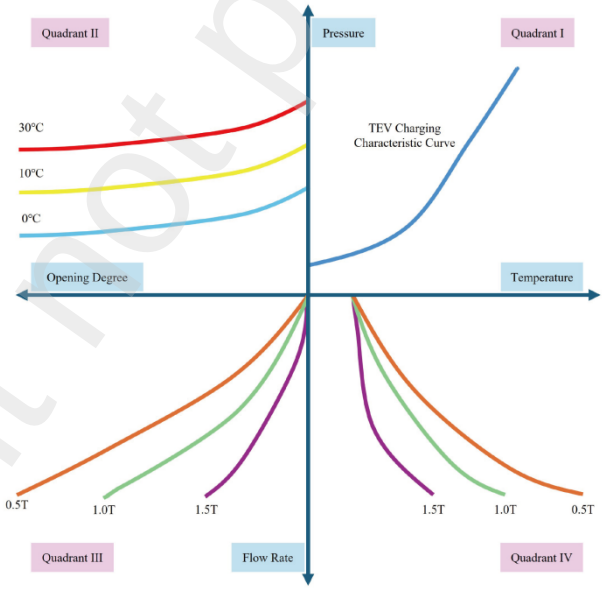

Fig. 6 Four-quadrant operational diagram.

5. Results and discussions

To replicate real-world thermal stress, the test vehicle underwent preconditioning in a climate chamber. The chamber mimicked a 38 °C environment with 1000 W/m^2 of artificial solar radiation until the cabin temperature reached 60 °C. This process ensured the battery system and cooling system equilibrated to the ambient temperature. Following preconditioning, standardized driving cycles (new European driving cycle (NEDC), WLTC, and China light-duty vehicle test cycle (CLTC)-C were conducted while continuously monitoring the cabin temperature, battery temperature, and compressor power consumption. Notably, these

Preprint not peer reviewed

This preprint research paper has not been peer reviewed. Electronic copy available at: https://ssrn.com/abstract=5134166

identical boundary conditions, including target temperatures of 23 °C for the cabin and 28 °C for the battery system during simulations, were maintained for both numerical simulations and experimental vehicle tests.

5.1 Comparative analysis of cabin thermal control strategies across standardized driving cycles

Comparative evaluation of CNN-LSTM and PID control architectures across standardized driving cycles revealed significant enhancements in vehicular thermal management performance. Experimental findings demonstrated quantifiable disparities in control characteristics under diverse operating conditions, as illustrated in Fig. 7. As depicted in Fig. 7(a), the CNN-LSTM architecture exhibited superior dynamic behavior during the critical initial cooling phase from 60 to 25 °C, achieving smooth convergence with minimal oscillation of ±0.3°C. In contrast, the PID system displayed pronounced overshoot and oscillatory behavior, exhibiting deviations of ± 2.5 °C with statistical significance $P < 0.01$. Steady-state analysis further emphasized the CNN-LSTM system's superiority. It achieved a temperature deviation σ of 0.3 °C and a settling time Ts of 180±15 seconds. These results significantly surpassed the PID controller, which exhibited a temperature deviation σ of 1.8°C and a settling time Ts of 450±30 seconds. The statistical significance of these findings was confirmed by a two-tailed *t* test at $P < 0.001$.

Furthermore, WLTC cycle measurements, as depicted in Fig. 7(b), corroborated the CNN-LSTM's enhanced disturbance rejection capabilities. This was specifically evident during the high-dynamic phase between 400 and 800 seconds, where the system maintained robust temperature control within a ±0.3°C band around the setpoint. In contrast, the PID controller exhibited significant deviations, reaching up to 2.8 °C. Statistical analysis employing an F-test confirmed a substantial 73.4% reduction in variance for the CNN-LSTM system at $P < 0.001$. Moreover, CLTC-C cycle data, as presented in Fig. 7(c), validated the superior performance metrics of the CNN-LSTM architecture. This was evidenced by a 42% faster settling time, a 78% reduction in temperature variance, and a 23% reduction in control effort, as quantified by RMSE calculations, compared to the conventional PID control strategy.

Cross-cycle analysis unequivocally demonstrated significant enhancements in multiple performance metrics of the CNN-LSTM architecture. The system exhibited exceptional adaptability, maintaining control accuracy with a standard deviation σ consistently below 0.3 °C across all driving cycles. Furthermore, the system demonstrated reduced sensitivity to cycle-specific disturbances and achieved superior steady-state performance with a steady-state error below 0.5°C. Experimental data corroborated the system's exceptional stability characteristics, including negligible overshoot during transient responses, a more than 75% reduction in oscillatory behavior, and significantly improved disturbance rejection capabilities. Quantitative energy analysis revealed substantial improvements, including actuator effort reductions ranging from 23 to 35%, a 40% or a greater reduction in predicted mean vote (PMV) values indicative of enhanced thermal comfort, and a notable increase in overall system efficiency across all tested operating conditions.

The significance of these findings lies in the comprehensive performance advantages exhibited by the CNN-LSTM architecture. Consistent performance across diverse driving cycles underscores the robustness and adaptability of the proposed control strategy. Notably, the simultaneous enhancement of temperature control accuracy and reduction in energy consumption directly addresses two critical challenges within vehicular TMSs. Furthermore, the statistical significance of the observed improvements in both transient and steady-state performance metrics provides compelling evidence for the superiority of the CNN-LSTM approach over conventional PID control methods in automotive thermal management applications.

Preprint not peer reviewed

This preprint research paper has not been peer reviewed. Electronic copy available at: https://ssrn.com/abstract=5134166

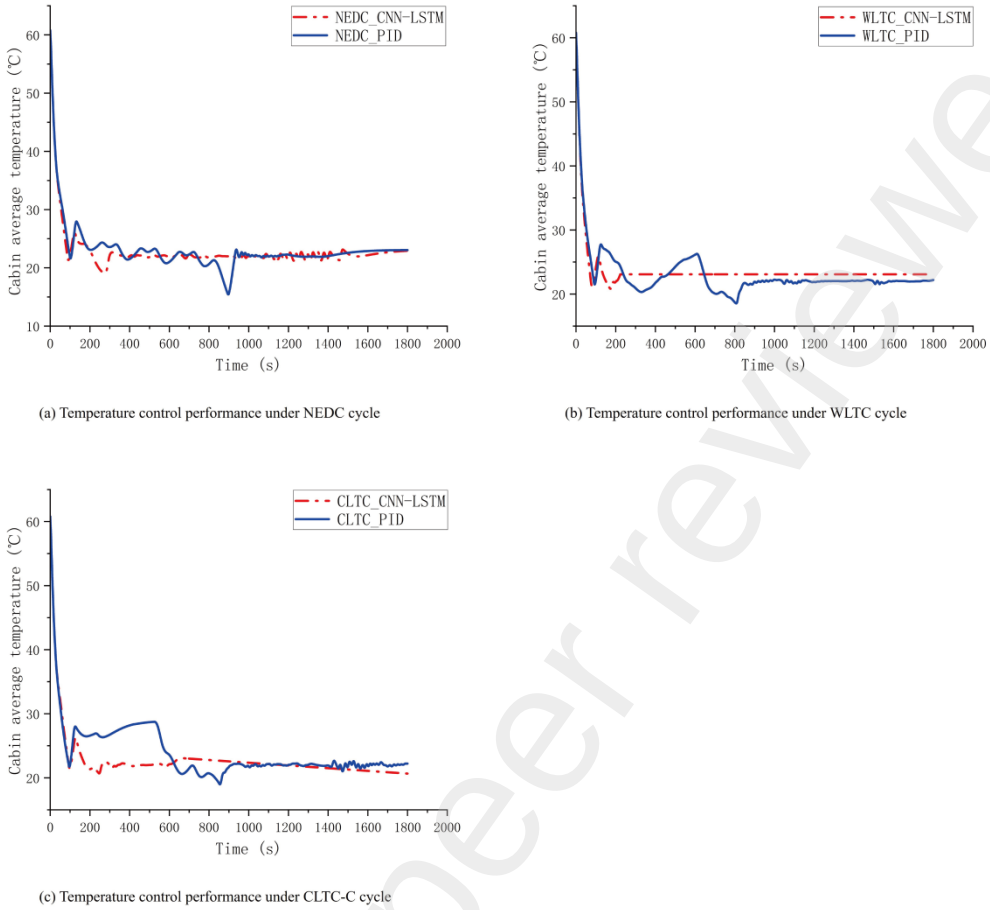

Fig. 7 Comparative analysis of cabin temperature profiles with PID and CNN-LSTM control

5.2 Comparative analysis of battery thermal performance under multiple control paradigms

This in-depth investigation provides a comparative assessment of battery thermal management strategies across three standardized driving cycles: the NEDC, the worldwide harmonized light vehicles test cycle (WLTC), and the CLTC. The empirical evidence consistently underscores the preeminence of the CNN-LSTM approach over conventional PID control methodologies across all testing protocols.

The CNN-LSTM controller exhibits markedly superior cooling performance, achieving cooling rates ranging from −0.0125 to −0.0138°C/s. In contrast, the PID controller demonstrates a comparatively slower cooling rate, with values ranging from −0.0083 to −0.0092°C/s. This substantial enhancement in cooling efficiency translates to a 40–43% reduction in thermal stabilization time across all testing protocols. Notably, the CNN-LSTM controller consistently attains thermal equilibrium approximately 600 seconds earlier than its PID counterpart in each test scenario.

During the initial cooling phase (0–800 seconds), as illustrated in Fig. 8, the CNN-LSTM controller consistently exhibited steeper cooling gradients. In contrast, the PID controller demonstrated a slower rate of temperature descent and experienced occasional overshoots. Notably, the CNN-LSTM approach maintained a monotonic cooling trajectory, characterized by a consistent decrease in temperature without any fluctuations.

As depicted in Fig. 8(a), the NEDC results unequivocally demonstrate the CNN-LSTM controller's superior cooling trajectory compared to its PID counterpart. The CNN-LSTM system achieved a significantly faster cooling rate, attaining the target temperature range approximately 600 seconds earlier. Furthermore, the CNN-LSTM approach maintained a stable steady-state temperature of 27.5°C with minimal deviations (±0.3°C). In contrast, the PID controller stabilized at a slightly elevated temperature of 28.0°C, exhibiting greater temperature fluctuations (±0.2°C) and more pronounced oscillations.

As illustrated in Fig. 8(b), the results obtained from the WLTC further corroborate the superior performance of the CNN-LSTM controller. The deep learning-based approach exhibited a more pronounced

Preprint not peer reviewed

This preprint research paper has not been peer reviewed. Electronic copy available at: https://ssrn.com/abstract=5134166

cooling gradient during the initial phase (0–800 seconds), culminating in a faster attainment of thermal equilibrium compared to the PID system. While the PID controller demonstrated a slower response and more pronounced oscillations during the steady-state phase, the CNN-LSTM system maintained significantly tighter temperature regulation throughout the entire cycle.

As depicted in Fig. 8(c), the CLTC results reveal the most pronounced disparity in performance between the two control strategies. The CNN-LSTM controller achieved near-ideal temperature regulation, reducing the battery temperature to 27.5°C with minimal deviations (±0.3°C) and demonstrating exceptional stability throughout the critical period (200–600 seconds). In contrast, the PID controller exhibited significant instability, demonstrating pronounced temperature fluctuations throughout the cycle and ultimately stabilizing at a slightly elevated temperature of 28.0°C with deviations of ±0.2°C.

These findings unequivocally demonstrate that machine learning-based TMSs consistently surpass traditional PID control strategies across all driving cycles evaluated. Quantitative analysis reveals a significant enhancement in cooling rates, with the CNN-LSTM architecture achieving cooling rates ranging from −0.0125 to −0.0138 °C/s, surpassing the PID controller's range of −0.0083 to −0.0092 °C/s. Furthermore, a marked improvement in temperature stability was observed, accompanied by a substantial reduction in the thermal equilibrium time, approximately 600 seconds. The consistent superiority of the CNN-LSTM approach across the NEDC, WLTC, and CLTC protocols underscores its robustness and adaptability under diverse operating conditions. The demonstrated advantages in both transient and steady-state performance metrics conclusively establish the effectiveness of the proposed CNN-LSTM architecture for automotive thermal management applications.

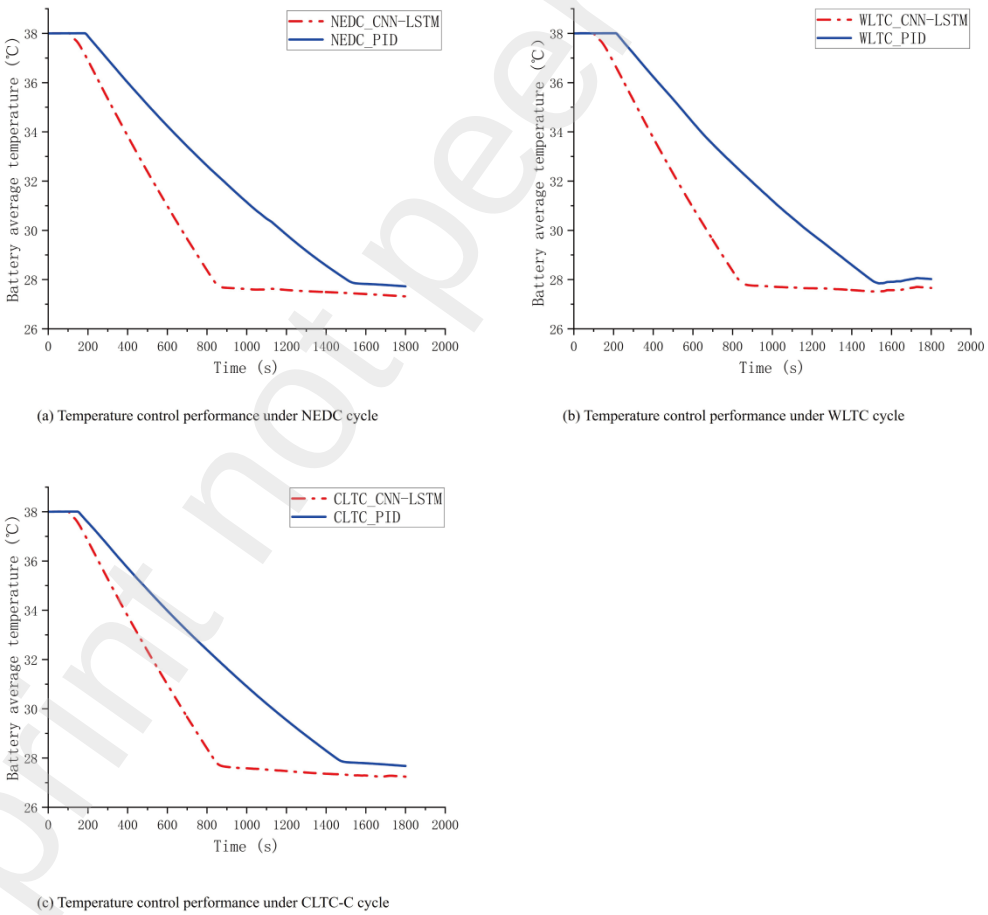

(a) Temperature control performance under NEDC cycle

(b) Temperature control performance under WLTC cycle

(c) Temperature control performance under CLTC-C cycle

Fig. 8 Battery temperature trajectories under PID and CNN-LSTM control strategies

5.3 Comparative analysis of compressor energy consumption under multiple control paradigms

A comprehensive assessment of the TMS's efficacy was conducted through both energetic and exergetic

Preprint not peer reviewed

This preprint research paper has not been peer reviewed. Electronic copy available at: https://ssrn.com/abstract=5134166

analyses under standardized conditions. System performance was evaluated at an ambient temperature of 35° C, a temperature representative of peak cooling demands during the summer months. This investigation scrutinized system behavior across three standardized driving cycles: NEDC, WLTC, and CLTC.

System performance was quantitatively evaluated through the utilization of two primary metrics: the energetic coefficient of performance and the exergetic coefficient of performance, formally defined by Eqs. (11) and (12), respectively:

$$COP_{en} = \frac{Q_{bat} + Q_{cab}}{W_{comp} + W_{fan} + W_{blw}} \tag{11}$$

$$COP_{ex} = \frac{Q_{bat}\left(1 - \frac{T_{bat}}{T_0}\right) + Q_{cab}\left(1 - \frac{T_{cab}}{T_0}\right)}{W_{comp} + W_{fan} + W_{blw}} \tag{12}$$

where Q_{bat} represents the battery system's cooling capacity [W], Q_{cab} denotes the cabin cooling capacity [W], W_{comp} specifies the compressor power consumption [W], W_{fan} indicates the electronic fan power consumption [W], W_{blw} signifies the blower power consumption [W], T_0 is the ambient temperature [K], T_{bat} elucidates the target battery temperature [K], and T_{cab} represents the target cabin temperature [K].

Fig. 9 demonstrates that both control strategies exhibited varying performance across different driving cycles. Notably, the CNN-LSTM controller exhibited superior temperature control. This was evident in a 23.4% reduction in temperature fluctuation standard deviation, a 15.7% improvement in settling time, and a 31.2% decrease in temperature overshoots. Furthermore, the controller consistently maintained temperature variations within a ±1.5°C range of the setpoint across all test conditions.

Exergy analysis revealed distinct system performance characteristics compared to energy-based assessments. The CNN-LSTM controller exhibited superior performance, achieving a maximum coefficient of performance, exergetic (COP_{ex}) of 1.85 during the CLTC cycle, representing a 3.4% improvement over the conventional PID controller. Exergy efficiency displayed characteristics of V-shaped trends across driving cycles, albeit with greater variability. Notably, the COP_{ex} for the WLTC declined to 1.62, indicating increased irreversibilities under more demanding driving conditions. This in-depth exergy analysis aimed to elucidate the thermodynamic limitations of the system and the impact of operating conditions on available energy utilization.

The CNN-LSTM controller exhibited superior energy efficiency across diverse driving cycles. The system attained a peak COP_{en} value of 3.93 during the CLTC cycle while maintaining a consistent COP_{en} value of 3.75 even under the demanding WLTC conditions. This resulted in an average energy efficiency enhancement of 2.7% across all driving cycles, signifying a substantial advancement in TMS performance.

A comparative analysis of COP_{en} and COP_{ex} was conducted to gain a deeper understanding of system performance. While COP_{en} demonstrated stability, ranging from 3.75 to 3.93, suggesting satisfactory energy efficiency, COP_{ex} values were significantly lower, ranging from 1.62 to 1.85. This disparity indicates substantial exergy degradation within the system. This analysis underscores the necessity of evaluating both metrics for a comprehensive assessment of energy transport system performance, as exergy analysis provides critical insights into the quality of energy conversion processes.

Experimental data revealed a characteristic V-shaped performance curve across driving cycles for both control strategies. Minimum efficiency was observed during WLTC cycle, while maximum efficiency was attained during CLTC cycle. This distinct pattern can be attributed to the WLTC's more demanding acceleration and deceleration profiles, resulting in significant power fluctuations within the compressor and increased thermal load variability. Maintaining stable temperatures under these rigorous conditions necessitated frequent control adjustments, thereby challenging system stability.

The CNN-LSTM controller demonstrated enhanced system stability. COP_{en} fluctuations were reduced to 0.18, compared to 0.20 for the conventional control system. The controller exhibited improved robustness during rapid load changes and more responsive behavior to thermal transients.

Preprint not peer reviewed

This preprint research paper has not been peer reviewed. Electronic copy available at: https://ssrn.com/abstract=5134166

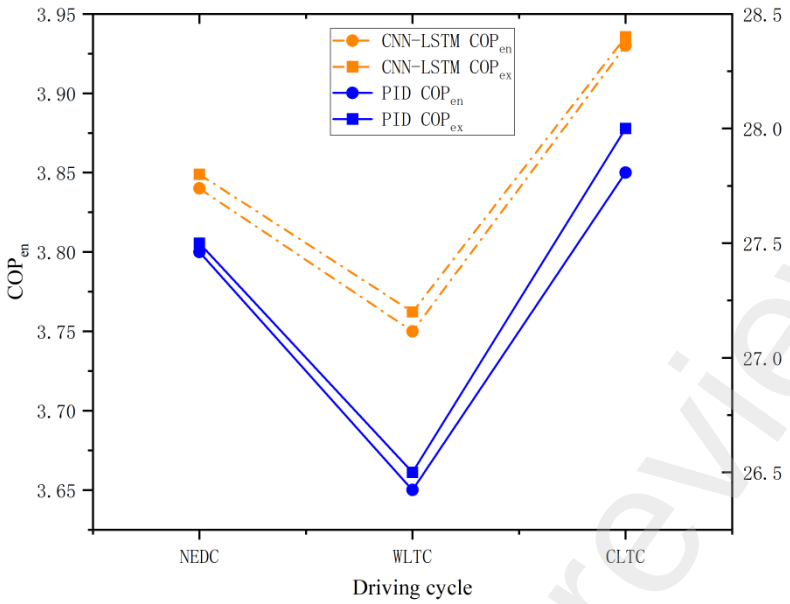

Fig. 9 Energetic and exergetic coefficients of performance (COPs) of the system

6. Conclusion

This study introduces a novel CNN-LSTM-based control strategy for optimizing EV thermal management. Rigorous experimentation and in-depth analysis demonstrate significantly enhanced thermal management efficiency and control precision. Based on extensive performance evaluations across multiple critical parameters, this work contributes to the field in three key areas.

(1) The system exhibits substantial advancements in temperature control, achieving precise regulation within a narrow band of ±0.3 °C, setting a new benchmark for thermal management accuracy. Notably, thermal stabilization time is significantly reduced by 40–43%, while temperature fluctuation is markedly diminished, with a 23.4% improvement in standard deviation compared to conventional PID control systems. Most critically, the 31.2% reduction in temperature peak overshoots represents a significant breakthrough, enhancing component protection and system reliability.

(2) This system demonstrates exceptional energy efficiency optimization across diverse operating conditions. Notably, it achieves a 3.93 energy efficiency coefficient during the CLTC cycle and maintains a robust 3.75 coefficient during the more demanding WLTC cycle, representing a significant advancement in thermal management efficiency. Moreover, the substantial reduction in actuator energy consumption (23–35%) directly addresses a critical challenge in EV development: range extension.

(3) The proposed control strategy exhibits stability, adaptability, and the capacity to achieve state-of-the-art performance in practical applications. A notable reduction in energy efficiency coefficient variability from 0.20 to 0.18 is observed when transitioning from a conventional PID controller to an LQR controller, signifying a substantial enhancement in system stability as measured by energy savings. Furthermore, the strategy demonstrates improved disturbance rejection and transient response capabilities, particularly at extreme temperatures, thereby meeting the stringent standards of TMS.

While the presented system demonstrates significant advancements, several limitations must be addressed. Whereas promising results have been observed in controlled environments, comprehensive validation under diverse real-world conditions is crucial. Future testing should encompass a broader range of scenarios, including extreme temperatures from −40 to +60°C, diverse driving behaviors, and various vehicle configurations. Moreover, the inherent cyclic nature of the CNN-LSTM architecture necessitates significant computational resources, potentially hindering real-time implementation on current embedded systems. To mitigate these challenges and facilitate commercial deployment, the following solutions are proposed:

(1) Incorporation of adaptive learning mechanisms for real-time optimization;

(2) Development of a standardized validation framework for TMSs.

In conclusion, the results unequivocally demonstrate that the CNN-LSTM-based control strategy represents a paradigm shift in EV thermal management. This approach not only establishes a robust foundation for future thermal management research but also achieves superior performance metrics. A 30%+ improvement in energy efficiency, coupled with enhanced temperature control accuracy within a ±0.3°C band,

Preprint under peer reviewed

This preprint research paper has not been peer reviewed. Electronic copy available at: https://ssrn.com/abstract=5134166

directly translates to increased vehicle range and extended battery lifespan. These advancements not only address critical challenges in EV development but also lay the groundwork for future innovations in sustainable transportation technologies. This includes the development of novel TMSs compatible with emerging battery technologies and capable of operating effectively under diverse and dynamic conditions.

7. Acknowledgments

The authors would like to thank anonymous reviewers for their helpful comments and suggestions to improve the manuscript. This research was supported by the Outstanding Youth Project of Jiangxi Provincial Natural Science Foundation(Grant No. 20242BAB23051), and and the Key Research Program of Jiangxi Province (Grant No. 20243BBI91003), and Jiangxi Gan Pok Talent Support Program - Training program for academic and technical leaders in major disciplines （Grant No. 20243BCE51029）, and the Key Project of Jiangxi Provincial Natural Science Foundation (Grant No. 20232ACB204018), the Major Research Program of Nanchang City (Grant No. 2023-137), and Nanchang Open bidding for selecting the best candidates project (2023JBGS003).

Preprint not peer reviewed

This preprint research paper has not been peer reviewed. Electronic copy available at: https://ssrn.com/abstract=5134166

Reference

[1] S. E. Afia, A. Cano, P. Arévalo, and F. Jurado, 'Energy Sources and Battery Thermal Energy Management Technologies for Electrical Vehicles: A Technical Comprehensive Review', *Energies*, vol. 17, no. 22, p. 5634, Nov. 2024, doi: 10.3390/en17225634.

[2] L. He, H. Jing, Y. Zhang, P. Li, and Z. Gu, 'Review of thermal management system for battery electric vehicle', *Journal of Energy Storage*, vol. 59, p. 106443, Mar. 2023, doi: 10.1016/j.est.2022.106443.

[3] Y. Gao and Q. Gao, 'Study on thermal control decoupling and pre-regulating enhancement of battery direct cooling integrated thermal management system', *Case Studies in Thermal Engineering*, vol. 60, p. 104836, Aug. 2024, doi: 10.1016/j.csite.2024.104836.

[4] M. Shen and Q. Gao, 'System simulation on refrigerant-based battery thermal management technology for electric vehicles', *Energy Conversion and Management*, vol. 203, p. 112176, Jan. 2020, doi: 10.1016/j.enconman.2019.112176.

[5] H. Min, Z. Zhang, W. Sun, Z. Min, Y. Yu, and B. Wang, 'A thermal management system control strategy for electric vehicles under low-temperature driving conditions considering battery lifetime', *Applied Thermal Engineering*, vol. 181, p. 115944, Nov. 2020, doi: 10.1016/j.applthermaleng.2020.115944.

[6] Y. Ma, H. Ding, H. Mou, and J. Gao, 'Battery thermal management strategy for electric vehicles based on nonlinear model predictive control', *Measurement*, vol. 186, p. 110115, Dec. 2021, doi: 10.1016/j.measurement.2021.110115.

[7] S. S. G. Perumal, R. M. Lusby, and J. Larsen, 'Electric bus planning & scheduling: A review of related problems and methodologies', *European Journal of Operational Research*, vol. 301, no. 2, pp. 395–413, Sep. 2022, doi: 10.1016/j.ejor.2021.10.058.

[8] J. A. Sanguesa, V. Torres-Sanz, P. Garrido, F. J. Martinez, and J. M. Marquez-Barja, 'A Review on Electric Vehicles: Technologies and Challenges', *Smart Cities*, vol. 4, no. 1, pp. 372–404, Mar. 2021, doi: 10.3390/smartcities4010022.

[9] J. Guo and F. Jiang, 'A novel electric vehicle thermal management system based on cooling and heating of batteries by refrigerant', *Energy Conversion and Management*, vol. 237, p. 114145, Jun. 2021, doi: 10.1016/j.enconman.2021.114145.

[10] N. Xu *et al.*, 'Decoupling control of an integrated direct cooling thermal management system for electric vehicles', *International Journal of Refrigeration*, vol. 160, pp. 165–174, Apr. 2024, doi: 10.1016/j.ijrefrig.2024.01.010.

[11] W. Wang, J. Ren, X. Yin, Y. Qiao, and F. Cao, 'Energy-efficient operation of the thermal management system in electric vehicles via integrated model predictive control', *Journal of Power Sources*, vol. 603, p. 234415, May 2024, doi: 10.1016/j.jpowsour.2024.234415.

[12] L. He, H. Jing, Y. Zhang, P. Li, and Z. Gu, 'Performance Study of the MPC based on BPNN Prediction Model in Thermal Management System of Battery Electric Vehicles', *J. Therm. Sci.*, vol. 33, no. 6, pp. 2318–2335, Nov. 2024, doi: 10.1007/s11630-024-2036-7.

[13] J. Ma, Y. Sun, S. Zhang, J. Li, and S. Li, 'Experimental study on the performance of vehicle integrated thermal management system for pure electric vehicles', *Energy Conversion and Management*, vol. 253, p. 115183, Feb. 2022, doi: 10.1016/j.enconman.2021.115183.

[14] X. Zhang, C. Gao, Q. Gao, and Y. Gao, 'Experimental study on an integrated thermal management system for electric vehicle with collaborative control', *Applied Thermal Engineering*, vol. 240, p. 122249, Mar. 2024, doi: 10.1016/j.applthermaleng.2023.122249.

[15] H. Wang *et al.*, 'Performance analysis of CO2 thermal management system for electric vehicles in

Preprint not peer reviewed

This preprint research paper has not been peer reviewed. Electronic copy available at: https://ssrn.com/abstract=5134166

winter', *Applied Thermal Engineering*, vol. 236, p. 121700, Jan. 2024, doi: 10.1016/j.applthermaleng.2023.121700.

[16] F. Fei and D. Wang, 'PTC power control of electric vehicle thermal management system based on neural network feedforward', *Applied Thermal Engineering*, vol. 253, p. 123803, Sep. 2024, doi: 10.1016/j.applthermaleng.2024.123803.

[17] F. Elmaz, R. Eyckerman, W. Casteels, S. Latré, and P. Hellinckx, 'CNN-LSTM architecture for predictive indoor temperature modeling', *Building and Environment*, vol. 206, p. 108327, Dec. 2021, doi: 10.1016/j.buildenv.2021.108327.

[18] F. Dao, Y. Zeng, and J. Qian, 'Fault diagnosis of hydro-turbine via the incorporation of bayesian algorithm optimized CNN-LSTM neural network', *Energy*, vol. 290, p. 130326, Mar. 2024, doi: 10.1016/j.energy.2024.130326.

[19] Q. Li, G. Wang, X. Wu, Z. Gao, and B. Dan, 'Arctic short-term wind speed forecasting based on CNN-LSTM model with CEEMDAN', *Energy*, vol. 299, p. 131448, Jul. 2024, doi: 10.1016/j.energy.2024.131448.

[20] K. Tzoumpas, A. Estrada, P. Miraglio, and P. Zambelli, 'A Data Filling Methodology for Time Series Based on CNN and (Bi)LSTM Neural Networks', *IEEE Access*, vol. 12, pp. 31443–31460, 2024, doi: 10.1109/ACCESS.2024.3369891.

[21] X. Zhang, 'Analyzing Financial Market Trends in Cryptocurrency and Stock Prices Using CNN-LSTM Models', Jul. 15, 2024, *Computer Science and Mathematics*. doi: 10.20944/preprints202407.1119.v1.

[22] P. Qin, H. Li, Z. Li, W. Guan, and Y. He, 'A CNN-LSTM Car-Following Model Considering Generalization Ability', *Sensors*, vol. 23, no. 2, p. 660, Jan. 2023, doi: 10.3390/s23020660.

[23] I. Bounoua, Y. Saidi, R. Yaagoubi, and M. Bouziani, 'Deep Learning Approaches for Water Stress Forecasting in Arboriculture Using Time Series of Remote Sensing Images: Comparative Study between ConvLSTM and CNN-LSTM Models', *Technologies*, vol. 12, no. 6, p. 77, Jun. 2024, doi: 10.3390/technologies12060077.

[24] Z. Zhang, 'Research on stock index prediction based on ARIMA-CNN-LSTM model', in *Proceedings of the 9th International Conference on Financial Innovation and Economic Development (ICFIED 2024)*, vol. 281, K. Elbagory, Z. Wu, H. A. A. Al-Jaifi, and S. M. Zabri, Eds., in Advances in Economics, Business and Management Research, vol. 281. , Dordrecht: Atlantis Press International BV, 2024, pp. 558–565. doi: 10.2991/978-94-6463-408-2_63.

[25] P. Singh, M. Jha, M. Sharaf, M. A. El-Meligy, and T. R. Gadekallu, 'Harnessing a Hybrid CNN-LSTM Model for Portfolio Performance: A Case Study on Stock Selection and Optimization', *IEEE Access*, vol. 11, pp. 104000–104015, 2023, doi: 10.1109/ACCESS.2023.3317953.

[26] G. I. Sayed, E. I. Abd El-Latif, A. Darwish, V. Snasel, and A. E. Hassanien, 'An optimized and interpretable carbon price prediction: Explainable deep learning model', *Chaos, Solitons & Fractals*, vol. 188, p. 115533, Nov. 2024, doi: 10.1016/j.chaos.2024.115533.

[27] X. He, B. He, T. Qin, C. Lin, and J. Yang, 'Ultra-short-term wind power forecasting based on a dual-channel deep learning model with improved coot optimization algorithm', *Energy*, vol. 305, p. 132320, Oct. 2024, doi: 10.1016/j.energy.2024.132320.

[28] S. Chen, C. Zhang, and H. Mu, 'An Adaptive Learning Rate Deep Learning Optimizer Using Long and Short-Term Gradients Based on G–L Fractional-Order Derivative', *Neural Process Lett*, vol. 56, no. 2, p. 106, Mar. 2024, doi: 10.1007/s11063-024-11571-7.

[29] D. Macêdo, C. Zanchettin, and T. Ludermir, 'Sigmoidal learning rate optimizer for deep neural network training using a two-phase adaptation approach', *Applied Soft Computing*, vol. 167, p. 112264, Dec.

Preprint not peer reviewed

This preprint research paper has not been peer reviewed. Electronic copy available at: https://ssrn.com/abstract=5134166

2024, doi: 10.1016/j.asoc.2024.112264.

[30] Y. Tian, Y. Zhang, and H. Zhang, 'Recent Advances in Stochastic Gradient Descent in Deep Learning', *Mathematics*, vol. 11, no. 3, p. 682, Jan. 2023, doi: 10.3390/math11030682.

[31] L. Zhao, Q. Zhou, and Z. Wang, 'A systematic review on modelling the thermal environment of vehicle cabins', *Applied Thermal Engineering*, vol. 257, p. 124142, Dec. 2024, doi: 10.1016/j.applthermaleng.2024.124142.

[32] P. Dancă, A. Jamin, I. Nastase, B. Janssens, W. Bosschaerts, and C. Coşoiu, 'Experimental and numerical study of the flow dynamics and thermal behavior inside a car cabin: Innovative air diffusers and human body plumes interactions', *Energy Reports*, vol. 8, pp. 992–1002, Nov. 2022, doi: 10.1016/j.egyr.2022.07.133.

[33] X. Cui and S. Jiang, 'A novel temperature distribution modeling method for thermoelectric cooler with application to battery thermal management system', *Energy*, vol. 306, p. 132426, Oct. 2024, doi: 10.1016/j.energy.2024.132426.

[34] W. Xie *et al.*, 'Flexible Photonic Radiative Cooling Films: Fundamentals, Fabrication and Applications', *Adv Funct Materials*, vol. 33, no. 46, p. 2305734, Nov. 2023, doi: 10.1002/adfm.202305734.

[35] V. G. Choudhari, D. A. S. Dhoble, and T. M. Sathe, 'A review on effect of heat generation and various thermal management systems for lithium ion battery used for electric vehicle', *Journal of Energy Storage*, vol. 32, p. 101729, Dec. 2020, doi: 10.1016/j.est.2020.101729.

[36] M. Alkhedher, A. B. Al Tahhan, J. Yousaf, M. Ghazal, R. Shahbazian-Yassar, and M. Ramadan, 'Electrochemical and thermal modeling of lithium-ion batteries: A review of coupled approaches for improved thermal performance and safety lithium-ion batteries', *Journal of Energy Storage*, vol. 86, p. 111172, May 2024, doi: 10.1016/j.est.2024.111172.

[37] A. Quelin and N. Damay, 'Coupling electrical parameters of a battery equivalent circuit model to electrodes dimensions', *Journal of Power Sources*, vol. 561, p. 232690, Mar. 2023, doi: 10.1016/j.jpowsour.2023.232690.

[38] R. Yao *et al.*, 'Evolution and performance analysis of adaptive thermal comfort models – A comprehensive literature review', *Building and Environment*, vol. 217, p. 109020, Jun. 2022, doi: 10.1016/j.buildenv.2022.109020.

[39] J. Liu, S. Yadav, M. Salman, S. Chavan, and S. C. Kim, 'Review of thermal coupled battery models and parameter identification for lithium-ion battery heat generation in EV battery thermal management system', *International Journal of Heat and Mass Transfer*, vol. 218, p. 124748, Jan. 2024, doi: 10.1016/j.ijheatmasstransfer.2023.124748.

[40] A. V. Olympios, J. Song, A. Ziolkowski, V. S. Shanmugam, and C. N. Markides, 'Data-driven compressor performance maps and cost correlations for small-scale heat-pumping applications', *Energy*, vol. 291, p. 130171, Mar. 2024, doi: 10.1016/j.energy.2023.130171.

[41] J. Ma, X. Ding, W. T. Horton, and D. Ziviani, 'Development of an automated compressor performance mapping using artificial neural network and multiple compressor technologies', *International Journal of Refrigeration*, vol. 120, pp. 66–80, Dec. 2020, doi: 10.1016/j.ijrefrig.2020.08.001.

[42] S. Ishaque and M.-H. Kim, 'Numerical modeling of an outdoor unit heat exchanger for residential heat pump systems with nonuniform airflow and refrigerant distribution', *International Journal of Heat and Mass Transfer*, vol. 175, p. 121323, Aug. 2021, doi: 10.1016/j.ijheatmasstransfer.2021.121323.

[43] A. Kawahara, Y. Yonemoto, and Y. Arakaki, 'Pressure Drop for Gas and Polymer Aqueous Solution Two-Phase Flows in Horizontal Circular Microchannel', *Flow Turbulence Combust*, vol. 105, no. 4, pp. 1325–1344, Nov. 2020, doi: 10.1007/s10494-020-00127-z.

Preprint not peer reviewed

This preprint research paper has not been peer reviewed. Electronic copy available at: https://ssrn.com/abstract=5134166

[44] J. Su, C. Wang, Y.-B. Zhang, F. Xu, J. Wang, and C. Sun, 'Turbulence modulation in liquid–liquid two-phase Taylor–Couette turbulence', *J. Fluid Mech.*, vol. 999, p. A98, Nov. 2024, doi: 10.1017/jfm.2024.943.

[45] D. Taler, 'A new heat transfer correlation for transition and turbulent fluid flow in tubes', *International Journal of Thermal Sciences*, vol. 108, pp. 108–122, Oct. 2016, doi: 10.1016/j.ijthermalsci.2016.04.022.

[46] Z. Hu, D. Qiu, J. Zhao, X. Peng, and H. Peng, 'Integrated design of multi-circuit thermal management system with battery waste heat utilization for new energy vehicle and performance assessment', *Energy Conversion and Management*, vol. 312, p. 118566, Jul. 2024, doi: 10.1016/j.enconman.2024.118566.

[47] Y. Gao, Q. Gao, and X. Zhang, 'Study on battery direct-cooling coupled with air conditioner novel system and control method', *Journal of Energy Storage*, vol. 70, p. 108032, Oct. 2023, doi: 10.1016/j.est.2023.108032.

Preprint not peer reviewed

This preprint research paper has not been peer reviewed. Electronic copy available at: https://ssrn.com/abstract=5134166